

A Study of Second-Order Susceptibility in Digital Alloy-Grown InAs/AlSb Multiple Quantum Wells

Natalie D. Foster, Ann Kathryn Rockwell, Joshua Andrew McArthur, Bernardo S. Mendoza, Seth R. Bank, and Michael C. Downer*

A preliminary measurement of the second-order nonlinear optical susceptibility $\chi_{MQW}^{(2)}$ of symmetric, coupled, InAs/AlSb multiple quantum well (MQW) structures is acquired through optical second-harmonic generation (SHG) at fundamental wavelength 1.55 μm . High quality crystalline MQW structures of variable thickness and corresponding bulk AlSb control samples are achieved using a digital alloy epitaxial growth technique that avoids cluster formation and phase segregation. All samples are grown in between a GaSb cap and substrate layer. To isolate SHG from the MQW (or control) layers of interest from cap and substrate contributions, a multilayer optical response matrix model is built and independently tested by accurately reproducing linear reflectivity spectra. While a simplified response matrix analysis of SHG based solely on bulk $\chi^{(2)}$ s does not reproduce the distinct SHG responses of the two sets of samples, the inclusion of an additional interface SHG contribution leads to a successful fit of the data and implies $|\chi_{MQW}^{(2)}| \approx 4 |\chi_{AlSb}^{(2)}|$. The results demonstrate a proof-of-concept quantification of $\chi^{(2)}$ in symmetric MQWs and suggest the possibility of engineering $\chi^{(2)}$ in these structures, particularly with the introduction of well asymmetries.

1. Introduction

Since realization of the semiconductor quantum well (QW) and its superlattice form, the multiple quantum well (MQW) structure,^[1] bandgap engineering studies have emerged to support MQW applications in optoelectronics and optical communications.^[2–11] Engineering of the nonlinear optical properties of MQWs, in particular,

by tuning, e.g., their asymmetry,^[12–14] composition,^[6,15] and width^[16] has led to practical, tunable structures at infrared wavelengths.^[12,14] Gurnick and De Temple^[17] first observed engineered second-order optical nonlinearities in multilayered structures by growing asymmetric Al composition gradients in $\text{Al}_x\text{Ga}_{1-x}\text{As}$ layers to break centrosymmetry. Subsequent experiments engineered optical nonlinearities in III–V semiconductor QWs for, e.g., tunable emitters^[2,15,18] and optical switching devices.^[6] However, experimental values of their second-order nonlinear susceptibilities $\chi_{MQW}^{(2)}$ have not yet been reported. Recent interest in engineering large optical second order nonlinearities in complex QW systems^[19–21] invites a timely systematic study quantifying $\chi^{(2)}$.

One of the challenges in engineering $\chi_{MQW}^{(2)}$ reliably is imprecision in the growth process. Random alloy growth in molecular beam epitaxy (MBE), which deposits

atoms slowly and directly on the surface of a substrate,^[22] is a common method for growing III–V MQWs. However, crystal structure defects imposed by the miscibility gap limit its composition in quaternary MQWs such as AlInAsSb .^[23] Recently, a complementary digital alloy (DA) technique^[24] has enabled more reproducible epitaxial growth of As- and Sb-based multilayered semiconductor structures.^[8,9,25–27] DA growth alleviates complications from cluster formation^[28] by rapidly shuttering As and Sb effusion cells in an optimized, pre-programmed sequence. It also circumvents alloy miscibility limits by growing short, well-controlled periods of binary compounds in sequence to mimic the properties of bulk alloys.^[29] Moreover, Sb-based compounds offer desirable traits such as bandgap flexibility and ease of lattice-matching with common substrates such as GaSb or InP. Compared with traditional MBE-grown structures, DA-grown structures can exhibit stronger photoluminescence,^[30] reduced compositional drift,^[24,31] tunable emission,^[8,32] and improved avalanche photodiode performance.^[9,25,33,34] In the context of nonlinear optics, the complex layer stacking sequences and sophisticated compositional grading accessible with DA growth could enhance second-order nonlinear response through symmetry breaking of the layer sequence across multiple length scales. This technique could materialize recently investigated theoretical structures promising large optical nonlinearities, such as asymmetric multiple-step QWs^[35] and QW-coupled optomechanical microcavities.^[36]

N. D. Foster, M. C. Downer
Department of Physics
The University of Texas at Austin
2515 Speedway, Austin, TX 78712, USA
E-mail: downer@physics.utexas.edu

A. K. Rockwell, J. A. McArthur, S. R. Bank
Department of Electrical Engineering
The University of Texas at Austin
2501 Speedway, Austin, TX 78712, USA

B. S. Mendoza
Centro de Investigaciones en Optica
Lomas del Bosque 115, Lomas del Campestre, León, Gto. 37150, Mexico

 The ORCID identification number(s) for the author(s) of this article can be found under <https://doi.org/10.1002/adom.202102845>.

© 2022 The Authors. Advanced Optical Materials published by Wiley-VCH GmbH. This is an open access article under the terms of the Creative Commons Attribution License, which permits use, distribution and reproduction in any medium, provided the original work is properly cited.

DOI: 10.1002/adom.202102845

The primary motivation behind this work was to determine what $\chi_{\text{MQW}}^{(2)}$ values are achievable in As- and Sb-based MQWs grown with the DA technique. To our knowledge no previous measurements of optical nonlinearities in such materials exist. The present study focuses on symmetric QWs—here, N identical periods of InAs QWs with AlSb barriers,—in order to establish a baseline $\chi_{\text{MQW}}^{(2)}$ against which $\chi^{(2)}$ of asymmetric MQWs can be compared in future work. A secondary motivation was to establish a method for extracting $\chi_{\text{MQW}}^{(2)}$ that is sufficiently reliable to enable accurate comparisons among such differently structured DA-grown MQWs. The method is challenging because the MQW structures cannot be studied in (here, GaSb) and capped with thin oxidation-inhibiting layers (here also GaSb) that themselves have $\chi^{(2)}$ comparable in magnitude to $\chi_{\text{MQW}}^{(2)}$. Thus, $\chi_{\text{MQW}}^{(2)}$ must be deconvolved from $\chi^{(2)}$ of the substrate and cap layers. To accomplish this, we measured optical second harmonic generation (SHG) in reflection from a series of substrate-MQW-cap structures, all with identical substrate and cap, but different N (i.e., different thickness). This was compared with SHG from otherwise identical control samples in which MQW layers were replaced with uniform AlSb layers of the same thickness with known $\chi_{\text{AlSb}}^{(2)} = 100 \text{ pm V}^{-1}$. We then analyzed both data sets with a multilayer nonlinear optical response model^[37] in order to isolate $\chi^{(2)}$ of the layer of interest (MQWs or control) from background bulk contributions to SHG from substrate and cap.

This initial analysis attempt, however, did not reproduce observed SHG trends. On the other hand, by inferring an additional source of SHG, localized at one of the interfaces between the layer of interest and the cap, that interferes with SHG from the three bulk sources,^[38,39] we obtained a consistent fit to all SHG data and extracted a preliminary effective susceptibility $|\chi_{\text{MQW}}^{(2)}| \approx 4 |\chi_{\text{AlSb}}^{(2)}|$ for the entire MQW layer. This measurement result constitutes the main conclusions of this work. The experimental and analysis method used to obtain it, and the unexpected need for an interfacial non-bulk SHG source to explain the data constitute important secondary conclusions. The fourfold enhancement in $\chi^{(2)}$ of symmetric InAs/AlSb

MQWs with respect to bulk AlSb suggests rich opportunities in applying similar methodology to other DA-grown MQW structures in future work with larger sample sets.

2. Sample Characterization

The left-hand drawing in Figure 1a shows the structure of a set of five control samples grown using the DA technique. Two other AlSb control structures were grown to supply a range of thicknesses to aid in testing the multilayer optical response algorithm. The right-hand drawing in Figure 1a shows the structure of five complementary MQW samples, also grown using the DA technique, in which the AlSb layer was replaced with MQWs of identical thickness. N periods (where $N = 5, 6, 7, 10,$ and 15) of symmetric QW pairs, each consisting of an InAs-AlSb-InAs-AlSb growth sequence, are sandwiched between 30 nm thick AlSb buffers, which serve to enable growth of the structure on a GaSb substrate and capping with a 10 nm GaSb oxidation-inhibiting layer. The InAs QWs in each pair are 1.5 nm thick, and are separated by 1 and 30 nm AlSb wavefunction and period barriers, respectively. Two identical copies of $N = 6$ period samples were grown to evaluate repeatability of the sample structure and optical properties.

2.1. Optical Characterization

2.1.1. Linear Ellipsometry

The GaSb cap layer and buried AlSb and GaSb layers surrounding the MQWs of interest were unavoidable sources of background SHG. Accurate modeling of background SHG was essential for extracting an accurate $\chi_{\text{MQW}}^{(2)}$. This in turn required accurate knowledge of the thickness d_{cap} of the cap layer, which varied by as much as 30% from its nominal 10 nm value among different growth runs, and of the complex refractive indices of cap and buried AlSb layers, which

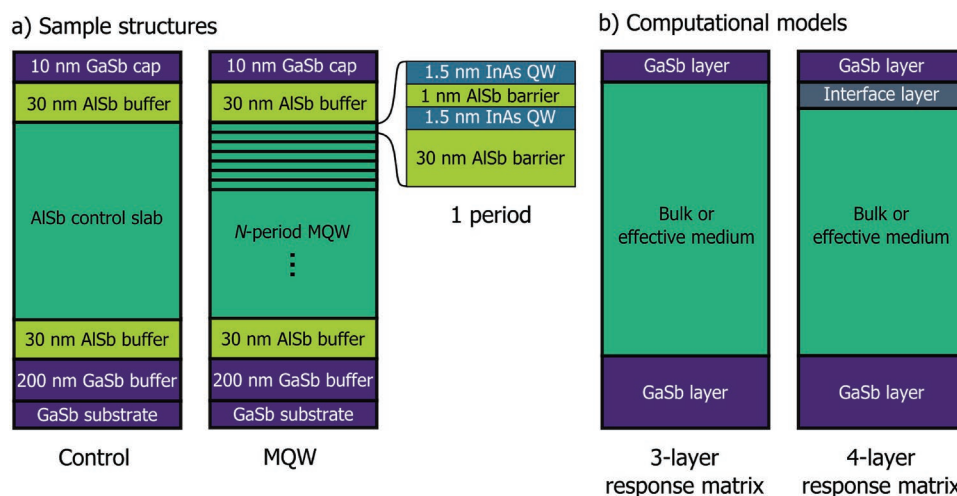


Figure 1. Sample structures and computational models. a) Structure of variable AlSb slab thickness control samples (left) next to their N -period MQW sample counterparts (right). Inset: internal structure of a single InAs-QW/AlSb-barrier period. b) Computational models of sample structures used for analyzing optical data: three-layer model for ellipsometry and preliminary SHG analysis (left); four-layer model including thin interface layer (right).

contribute to SHG Fresnel factors and determine the exponential attenuation of fundamental light intensity through the stack. To determine these parameters, we measured complex reflectance spectra of all samples over a spectral range that included fundamental and second-harmonic wavelengths. The three-layer model shown in the left-hand diagram of Figure 1b, consisting of a roughened GaSb cap layer of undetermined thickness, an effective monolithic intermediate layer and a GaSb substrate with predetermined refractive index, proved adequate for our purposes. Attempts to model the ellipsometry data with a more finely structured intermediate layer did not yield significantly different, nor demonstrably more accurate, cap and intermediate layer parameters, nor significantly different SHG modeling results from those presented below (see example raw and fitted ellipsometry spectra and derived linear optical spectra shown in Figures S1 and S2, Supporting Information; derived linear optical parameters and thickness shown in Table S1, Supporting Information).

2.1.2. Second-Harmonic Generation

For each sample, we measured SHG intensity in each of four polarization configurations—p-in/p-out, p-in/s-out, s-in/p-out, and s-in/s-out—as a function of azimuthal sample rotation angle ϕ around the surface normal. Here, $\phi = 0^\circ$ when the crystalline [100] axis lies in the plane of incidence. In these configurations, bulk SHG intensity varies sinusoidally, exhibiting four peaks of equal intensity over a full rotation, as observed for other [001]-oriented zinc blende III–V crystals of $\bar{4}3m$ symmetry.^[40,41] We nevertheless completed each azimuthal scan over a full 360° rotation to check peak height reproducibility. This confirmed stability of the rotation axis, focal plane, and laser parameters during each scan. Moreover, it provided an initial screening for the possible presence of unwanted azimuthally isotropic SHG contributions that, when significantly present, interfere with bulk. To ensure uniform excitation conditions from sample to sample, we dithered the sample plane with respect to the laser focus for each scan to maximize SHG intensity. In addition, we measured SHG from a coplanar reference GaAs sample translated temporarily into the focus, in order to normalize all signals against drifts in focused laser intensity at the sample surfaces.

3. Optical Response Matrix

We modeled the linear and nonlinear optical responses of our multilayer MQW and control samples using a transfer matrix formalism developed by Bethune.^[37] In this approach, a plane wave fundamental beam impinges on a structure consisting of multiple parallel nonlinear layers. Nonlinear source polarizations in the bulk of each layer, but not at the interfaces between them, generate the harmonic beam in the approximation that SHG contributes negligibly to pump depletion. Multiple reflections of both fundamental and harmonic beams are then taken into account via standard boundary conditions expressed as 2×2 transfer matrices whose elements are reflection and transmission amplitudes. As the fundamental and generated

harmonic beams propagate through the layered media, they acquire a phase factor proportional to the thickness traversed in each layer. The layers consist of cubic materials with isotropic linear optical properties and second order nonlinear susceptibilities with a single nonvanishing tensor component $\chi_{xyz}^{(2)}$. Since output fields are expressed as a sum of contributions from individual layers, the contribution of one layer of interest can be extracted when remaining layers are accurately modeled.

The second-order nonlinear polarization components used to represent the GaSb cap and substrate layers and the effective medium composed of either AlSb slab or MQWs are

$$P_{pp}^{(2)} = 3\epsilon_0 F_{pp} \chi^{(2)} \sin 2\phi \quad (1)$$

$$P_{ps}^{(2)} = -2\epsilon_0 F_{ps} \chi^{(2)} \cos 2\phi \quad (2)$$

$$P_{sp}^{(2)} = -\epsilon_0 F_{sp} \chi^{(2)} \sin 2\phi \quad (3)$$

where the subscripts on P and F refer to incoming and outgoing polarizations, and $F = F(n(\lambda_1), k(\lambda_1), n(\lambda_2), \text{and } k(\lambda_2))$ are the Fresnel coefficients. $\chi^{(2)} = \chi_{xyz}^{(2)}$ is the second-order nonlinear bulk susceptibility. We input linear optical constants at fundamental λ_1 and second-harmonic $\lambda_2 = \lambda_1/2$ that govern multiple reflections, attenuation and the SHG Fresnel factors from ellipsometry measurements (see Supporting Information Section S2 for more details).

We carried out two independent tests of our multilayer response matrix. First, as shown in Figure 2, we reproduced measured 45° -incidence angle p-polarized linear reflectivity spectra (black curves) of both control (Figure 2a) and MQW (Figure 2b) structures over the wavelength range $400 \leq \lambda \leq 1600$ nm through matrix calculations based on ellipsometry-derived refractive indices and absorption coefficients (green curves). Second, we reproduced the SHG results in a nonlinear layered structure from Teshima et al.,^[43] which employed a similar multilayer response matrix approach (see Figure S3, Supporting Information).

4. Results and Discussion

Figure 3 summarizes our ϕ -dependent SHG measurements (for cases not shown here, see Figure S4, Supporting Information). Figure 3a shows p- and s-polarized SHG from five control structures using a p-polarized fundamental beam; Figure 3b shows the same from corresponding MQW structures. The clear contrast between these SHG responses is *prima facie* qualitative evidence that $\chi_{MQW}^{(2)}$ differs significantly from $\chi_{AlSb}^{(2)}$. However, the raw data do not immediately reveal the quantitative relationship between $\chi_{MQW}^{(2)}$ and $\chi_{AlSb}^{(2)}$, because the signal of interest is homodyned with other SHG sources. Figure 3c shows p- and s-polarized SHG intensity from an $N = 5$ MQW structure due to s-polarized fundamental excitation, on an amplified vertical scale. This signal is not only significantly weaker than p-in SHG from this sample (Figure 3b, top panel), but s-in/p-out data (black) displays unequal peak heights, for which Equation 3 provides no basis.

In past work, such unequal peaks have been attributed to isotropic background SHG contributions (e.g., from defects

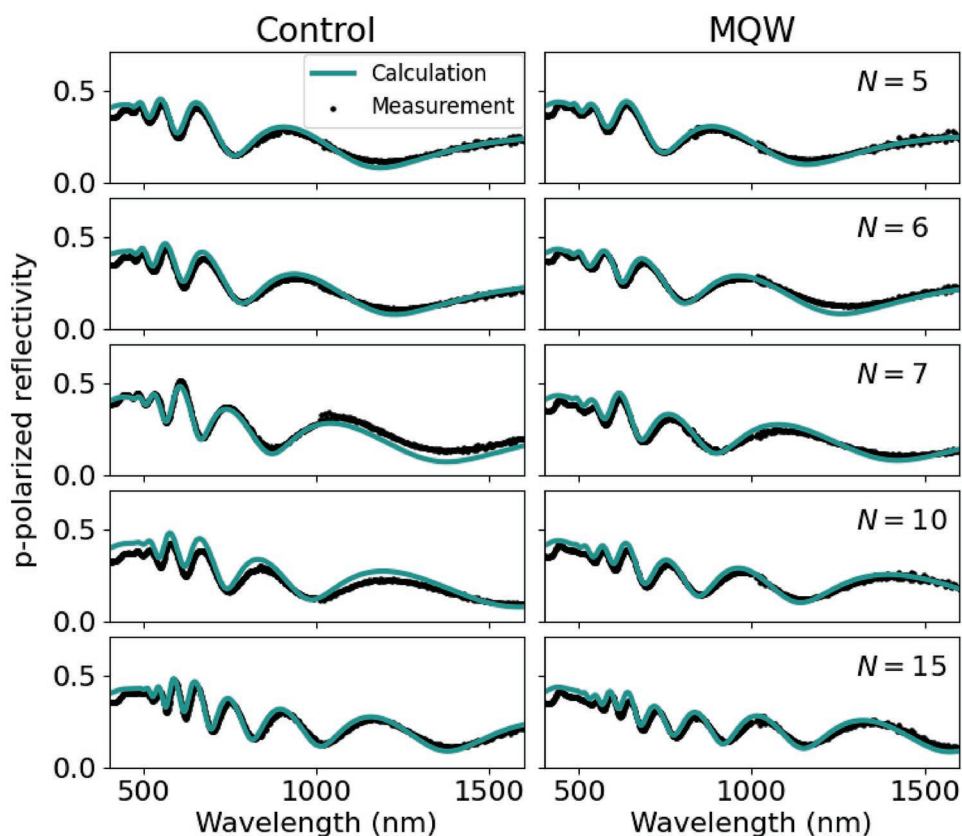


Figure 2. Measured and calculated p-polarized linear reflectivity spectra. a) Spectra for five AlSb control structures and for b) corresponding MQWs of the same thickness. Calculations (green curves) are generated by multilayer optical response matrix using ellipsometry-derived linear optical constants for individual layers.

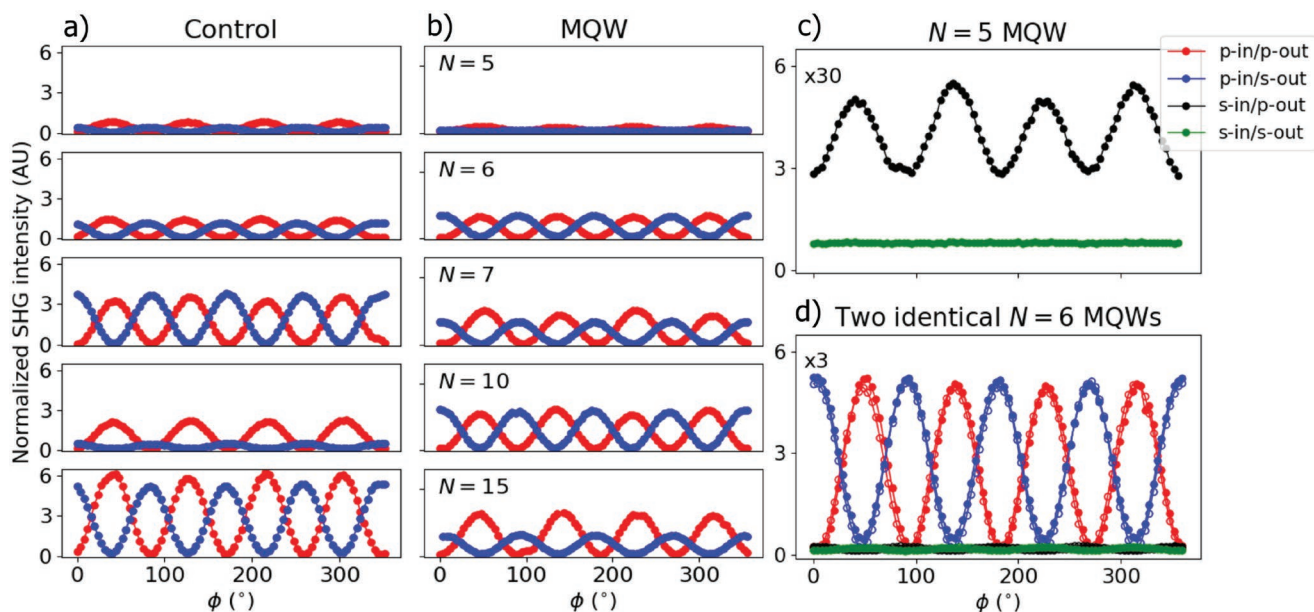


Figure 3. Dependence of normalized SHG intensity on azimuthal angle (ϕ). a,b) p- (red) and s-polarized (blue) SHG from a p-polarized fundamental beam for a) AlSb control structures and b) corresponding MQW with N repeated layers as shown. c) p- (black) and s-polarized (green) SHG intensity from a $N = 5$ MQW structure for an s-polarized fundamental beam. d) SHG from two identical copies of the $N = 6$ MQW structure, distinguished by open and filled markers.

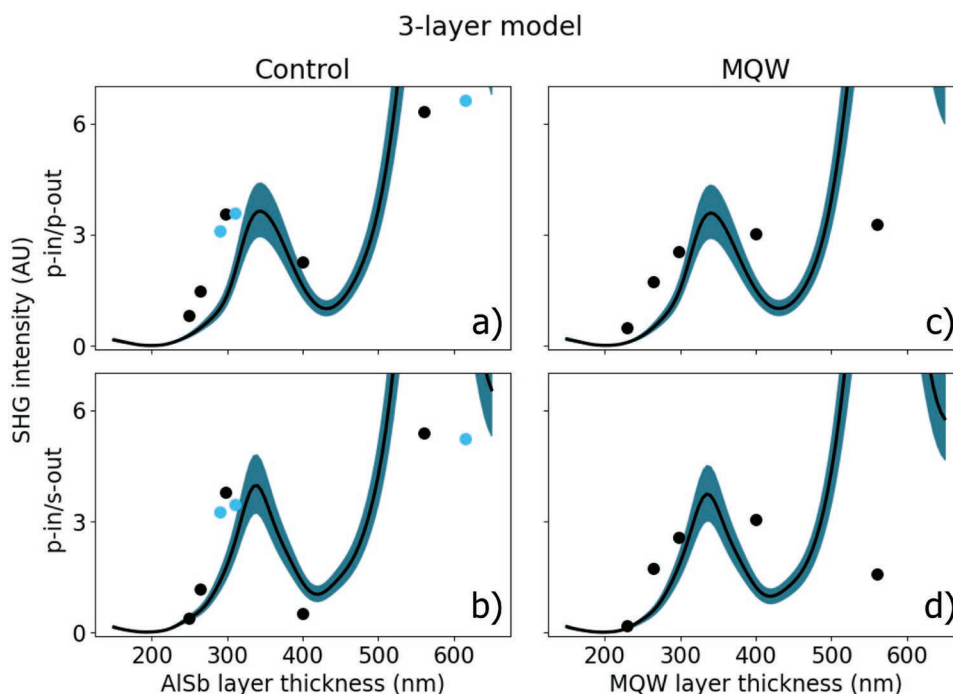


Figure 4. Three-layer optical response matrix calculations of total reflected SHG intensity. a,b) p-polarized fundamental excitation and resulting a) p- and b) s-polarized SHG calculations for AlSb control structures. The black scatter points are measured data indicating corresponding thickness control structures to the MQW structures shown in the right-hand side panels. c, d) p-polarized fundamental excitation and c) p- and d) s-polarized SHG calculations for MQWs. In all cases, the filled teal region defines a range within 10% of $\chi_{\text{bulk}}^{(2)} = 100 \text{ pm V}^{-1}$, which is denoted by the solid black line. Data points represent an average of the four maxima over 2π rotation in ϕ for each sample.

or surfaces) interfering with anisotropic bulk contributions.^[42] The s-in/s-out SHG signal (Figure 3c, green curve) is extremely weak and completely isotropic. It is forbidden for ideal [001] surfaces of III-V semiconductors, but can become weakly allowed when this surface is rough.^[44] This is a possible source of the isotropic SHG background that gives rise to unequal peak heights for s-in/p-out SHG. The absence of any anisotropic component to the s-in/s-out SHG signal—which can arise from polarization leakage—shows that polarization vectors are well-aligned with the plane of incidence (p-pol) or the surface plane (s-pol). Here, we will extract $\chi_{\text{MQW}}^{(2)}$ solely from the much stronger p-polarized SHG signals, which exhibit near-exact fourfold symmetry in accordance with Equation 1 and 2, indicating that isotropic SHG background can safely be neglected. We also established repeatability of the MQW structure growth process by growing two copies of the $N = 6$ structure, whose ϕ -dependent SHG shows nearly identical responses (Figure 3d).

As a first step in extracting a quantitative relationship between $\chi_{\text{AlSb}}^{(2)}$ and $\chi_{\text{MQW}}^{(2)}$, we calculated total SHG intensity from control and MQW samples as a function of thickness of the AlSb or MQW layers, respectively, using the 3-layer model depicted in the left-hand diagram of Figure 1b. Effective linear optical constants for the variable-thickness layers came from ellipsometry, and from literature^[45] for the GaSb layers. Literature values^[46] of the bulk nonlinear susceptibilities $\chi_{\text{GaSb}}^{(2)} \approx 800$ and $\chi_{\text{AlSb}}^{(2)} \approx 100 \text{ pm V}^{-1}$ were assigned with equal phases to the GaSb and AlSb layers, respectively, but allowed to vary $\pm 10\%$ to optimize the fit of calculated SHG intensity to the data.

From these assignments, we calculated SHG intensity from the control sample as a function of AlSb layer thickness d_{AlSb} (see Figure S5, Supporting Information for resulting calculation over the range $0 < d_{\text{AlSb}} < 10 \text{ }\mu\text{m}$). It was not feasible to grow samples over a wide d_{AlSb} range in fine enough increments, and with sufficient accuracy, to exhibit various interference fringes arising from multiple internal reflections. Instead, we concentrated sample growth in the range of the two lowest-order fringes since the calculations predicted clear d_{AlSb} -dependent SHG intensity, and the small d_{AlSb} values minimized growth time while maximizing growth accuracy.

Figure 4a,b shows the latter calculation results (solid curves) over the range of $200 < d_{\text{AlSb}} < 600 \text{ nm}$ (see fitting parameter results in Tables S2 and S3, Supporting Information). The first, and part of the stronger second, interference peaks that occur as d_{AlSb} increases from zero are visible. Teal shading shows the impact of up to $\pm 10\%$ variations in $\chi_{\text{AlSb}}^{(2)}$ from its literature value.

We grew six control samples in the range of $250 < d_{\text{AlSb}} < 400 \text{ nm}$ to map out the first interference fringe, and two in the $500 < d_{\text{AlSb}} < 600 \text{ nm}$ range, which coincides with the second. Black and blue data points show measured relative SHG intensities for p-in/p-out (Figure 4a) and p-in/s-out (Figure 4b) polarization, averaged over the four peak heights acquired over 2π azimuthal rotation. Black points denote control samples for which we grew a corresponding ($d_{\text{MQW}} = d_{\text{AlSb}}$) MQW sample. Full data sets were acquired on the sample set three times and spaced out over several months, which produced very similar trends. Error bars representing variation of SHG intensity for each sample are on the order of the size of the data points,

and are therefore not shown separately. The dominant source of error in our analysis originates from the response matrix calculation, denoted by the shaded teal region. We applied an overall vertical scaling factor to all 16 data points in Figure 4a,b to fit the shape of the calculated curves best, since absolute SH intensities could not be measured accurately. The data for the six smallest d_{AlSb} values indeed map out the first fringe fairly well, and agree with the predicted polarization-dependence, although the measured peak is slightly shifted from the calculated one. SHG was indeed stronger for the two largest d_{AlSb} values, but by roughly a factor of two less than the quantitative calculation predicted.

Figure 4c,d similarly compare three-layer model calculation results to SHG data for the MQW samples. Since, however, the 3-layer model treats the MQWs as a monolithic layer described by $\chi_{\text{eff}}^{(2)}$, and since overall SHG intensity from the five MQW samples was similar in magnitude to that from control samples, the calculated best-fit curves are nearly identical to those shown in Figure 4a,b, and correspond to a similar susceptibility $\chi_{\text{eff}}^{(2)} \approx \chi_{\text{AlSb}}^{(2)} \approx 100 \text{ pm V}^{-1}$. This model, however, fails to capture robust differences in thickness-dependent SHG between control and MQW samples that are clearly evident in the data.

These differences are most pronounced for the 400 nm ($N = 10$) and 570 nm ($N = 15$) samples. For the former, the control sample yielded much weaker s- than p-out SHG intensity, and both were weaker than for the next thinner sample; in contrast, the MQW sample yielded nearly equal s- and p-out intensities, both stronger than for the next thinner sample. For the latter, the reverse was true: the control sample yielded nearly equal s- and p-out intensities, the MQW sample weaker s-out. Moreover, the weak SHG response of the $N = 15$ MQW samples compared with thinner samples contradicts the strong second-order interference peak expected from the calculations. These and other more subtle discrepancies evident in Figure 4 indicated that the three-layer model underfitted the available data.

A straightforward extension is to disassemble the monolithic MQW layer into its constituent components shown in Figure 1b, assigning 30 nm AlSb buffer and inter-QW barrier layers $\chi_{\text{AlSb}}^{(2)}$ and individual QWs $\chi_{\text{QW}}^{(2)}$ as a fit parameter. However, this approach does not lead to substantial differences from, or improvements upon, the simpler three-layer analysis presented in Figure 4, and provides no physical insight into the discrepancies between calculations and data shown there.

We therefore considered the possibility that additional SHG sources exist within one or both sets of heterostructures that the three-layer model does not include. Hetero-interfaces are a prime candidate, since excess charge,^[47] and/or strain near, such interfaces can break centrosymmetry locally, creating a source of SHG^[48] that interferes with the bulk sources considered in the three-layer model. In both sets of samples, the GaSb/AlSb interface between cap and buffer is a possible source of an additional $\chi_{\text{eff}}^{(2)}$. In MQW samples the interface between buffer and MQW layer is another.

To explore this possibility, while minimizing the number of new parameters, we introduced the four-layer model shown on the far right side of Figure 1b). Here, a single “interface layer” between the GaSb cap and underlying AlSb or MQW layer represented the various possible SHG contributions from the interfacial regions described above. Our choice of placement

for the 4th layer was not arbitrary; we considered equally simple ways to implement the layer, such as in between the AlSb or MQW layer and the substrate, but, by contrast, they did not produce a satisfactory fit to the data. Further, previous works have quantified excess electron density at the interface of a GaSb cap layer and InAs/AlSb QWs,^[47] structures similar to our own. In principle, three parameters—thickness d_{int} and complex nonlinear susceptibility $\chi_{\text{int}}^{(2)} = |\chi_{\text{int}}^{(2)}| e^{i\delta}$ with magnitude $|\chi_{\text{int}}^{(2)}|$ and phase δ —could describe this layer. In practice, however, for the small $d_{\text{int}} \lesssim d_{\text{cap}}$ of interest here, interface layers of the same $d_{\text{int}} |\chi_{\text{int}}^{(2)}|$ product yielded identical calculated results. This reduced the effective number of new parameters to 2 for each sample group (control and MQW).

We assigned the interface layer the same linear optical constants as AlSb, on the grounds that no such layer was necessary to model linear optical results (see, e.g., Figure 2). Thus our four-layer model differed from our three-layer model only in its nonlinear optical properties. We then varied $\chi_{\text{AlSb}}^{(2)}$ (or $\chi_{\text{MQW}}^{(2)}$) together with $d_{\text{int}} |\chi_{\text{int}}^{(2)}|$ and δ to find the best fit to measured SHG intensity for $250 < d_{\text{eff}} < 600$ nm within each sample group. In practice, only when the interface layer generated an SH field $E_{\text{SH}}^{\text{int}}$ of magnitude comparable to that of the average SH field from the bulk layers did four-layer model predictions differ substantially from three-layer model predictions.

Figure 5 shows the best-fit results as solid curves overlaid with measured data points for control (left) and MQW (right) samples in p-in/p-out (top) and p-in/s-out (bottom) polarization, for the same range of AlSb (or MQW) layer thicknesses as in Figure 4 (see fitting parameter results in Tables S4 and S5, Supporting Information). Because of the additional SH-generating layer, additional sub-structure appears in the two primary interference fringes. This substructure varies between sample groups and polarizations in ways that remedy the main discrepancies seen with the three-layer model. Specifically, SHG from the 400 nm samples now corresponds to a satellite peak of the 1st interference fringe at $d_{\text{eff}} = 300$ nm. The calculated height and shape of this peak track variations in measured SHG intensity for this sample well. Additionally, SHG from 570 nm samples now corresponds to a minimum between two sub-peaks of the second interference fringe, rather than to the peak of the single fringe seen in Figure 4. The four-layer model accounts for its weaker-than-expected intensity and its polarization-dependence.

Simultaneously with these improvements, the centroid offset between measured and calculated first interference fringe peak position, evident in Figure 4, is corrected with the four-layer model. The statistical χ^2 values (not to be confused with $\chi^{(2)}$) of the best fits shown in Figure 5 are as small as obtained for fits of the linear optical properties of the two sample groups shown in Figure 2. Moreover, these χ^2 minima are unique within the parameter space of the four-layer model. Finally, they correspond to the best-fit effective susceptibilities $\chi_{\text{AlSb}}^{(2)} = 100 \pm 20 \text{ pm V}^{-1}$ for control samples and $\chi_{\text{MQW}}^{(2)} = 400 \pm 80 \text{ pm V}^{-1}$ for MQW samples. Considering that $\approx 90\%$ of the volume of the effective MQW layer consists of AlSb (see Figure 1a, right), the local $\chi^{(2)}$ of the QW material could be as high as 3000 pm V^{-1} , exceeding even the pm V^{-1} of bulk InAs, the material of which individual QWs are made. Here we have chosen to emphasize $\chi_{\text{MQW}}^{(2)}$ with respect to $\chi_{\text{AlSb}}^{(2)}$ because AlSb comprises the volume

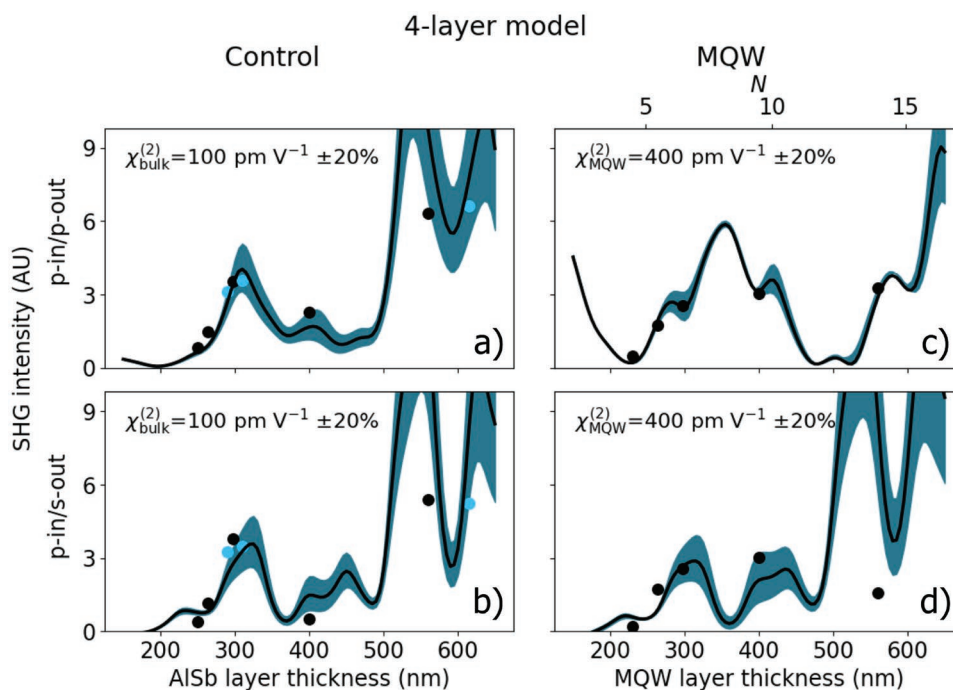


Figure 5. Four-layer optical response matrix calculations of total reflected SH intensity. a, b) p- and s-polarized fundamental excitation and resulting a) p- and b) s-polarized SHG calculations for ALSb control structures, where the filled teal region defines a range within 20% of $\chi_{\text{bulk}}^{(2)} = 100 \text{ pm V}^{-1}$. The black points are measured data indicating corresponding thickness control structures to the MQW structures shown in the right-hand side panels. c), d) p-polarized fundamental excitation and c) p- and d) s-polarized SHG calculations for MQWs, where the filled teal region defines a range within 20% of $\chi_{\text{MQW}}^{(2)} = 400 \text{ pm V}^{-1}$. The solid black lines are set the values shown in each panel. Data points represent an average of the four maxima over 2π rotation in ϕ for each sample.

majority of the MQW layer and it is also the reference material used for the control measurement. We note that although $\chi_{\text{MQW}}^{(2)} > \chi_{\text{ALSb}}^{(2)}$, apparently $I_{\text{MQW}}^{\text{SHG}} < I_{\text{ALSb}}^{\text{SHG}}$ for some cases shown in Figure 3a,b (e.g., for $N = 15$) due to destructive interference weakening the total SHG signal through the inclusion of δ in the layers.^[38] For example, $|\chi_{\text{int}}^{(2)} + \chi_{\text{ALSb}}^{(2)}|^2 > |\chi_{\text{int}}^{(2)} + \chi_{\text{MQW}}^{(2)}|^2$ when $2\chi_{\text{int}}^{(2)}(\chi_{\text{ALSb}}^{(2)}e^{i\delta_{\text{ALSb}}} + \chi_{\text{MQW}}^{(2)}e^{i\delta_{\text{MQW}}}) > |\chi_{\text{MQW}}^{(2)}|^2 - |\chi_{\text{ALSb}}^{(2)}|^2$, where δ_{ALSb} (δ_{MQW}) is the SH phase between the interface and ALSb (MQW) layers.

Nevertheless, the above conclusions must be treated as suggestive rather than definitive, for two reasons. First, the number of data points fit (seven for control samples, five for MQW samples) only marginally exceeds the number (3) of parameters varied. Much larger groups of samples with finer and wider distributions of d_{eff} will have to be grown in order to demonstrate the reliability of the extracted $\chi_{\text{MQW}}^{(2)}$ convincingly. Second, the physical nature of the hypothesized interface $\chi^{(2)}$ layer is not yet identified definitively, even though the existence of a $\chi^{(2)}$ source beyond purely bulk values is clear from the inability of the three-layer model to explain the data. Explanations other than the four-layer model in Figure 1b may therefore exist. Thus the global uniqueness of the best fit shown in Figure 5 cannot yet be guaranteed.

5. Conclusion

We have carried out measurements of linear and SHG reflectivity from DA-grown InAs/ALSb MQWs sandwiched between GaSb cap and substrate layers, and control samples with a

uniform ALSb layer replacing the MQWs, with the aim of determining $\chi_{\text{MQW}}^{(2)}$ relative to $\chi_{\text{ALSb}}^{(2)}$. We observed distinct linear and SHG optical responses from MQW and control sample sets, prima facie evidence that $\chi_{\text{MQW}}^{(1)}$ and $\chi_{\text{MQW}}^{(2)}$ differed from $\chi_{\text{ALSb}}^{(1)}$ and $\chi_{\text{ALSb}}^{(2)}$, respectively. A multilayer optical response matrix model, based on effective refractive indices of the constituent layers derived from ellipsometry, quantitatively reproduced linear reflectivity spectra as the MQW (or control ALSb) layer thickness varied. However, the consideration of effective bulk $\chi^{(2)}$ s in the same model was insufficient to quantitatively account for observed SHG trends. Only by inferring an additional interfacial SHG source with phase δ could the SHG responses of MQW and control samples be fit accurately. From this successful four-layer model fit, a preliminary value of $\chi_{\text{MQW}}^{(2)} \approx 400 \text{ pm V}^{-1} \approx 4\chi_{\text{ALSb}}^{(2)}$ was extracted. Our new findings in symmetric MQWs open the door to broad possibilities engineering $\chi^{(2)}$ in more complex MQW structures for optoelectronic applications. Future work will need to use significantly larger sample sets in order to ensure that $\chi^{(2)}$ values of MQW, control and interfacial layers are accurately and uniquely constrained. Nevertheless, the method developed here can effectively guide the engineering of optimized $\chi_{\text{MQW}}^{(2)}$ in more complex structures, such as asymmetric MQWs or even novel $\chi^{(3)}$ materials.

6. Experimental Section

Sample Growth: Samples were grown by a rapid-shuttering DA technique of solid-source MBE on n-type GaSb (001) substrates at a growth temperature of 460–°C, as determined by blackbody thermometry.^[8] Solid-source valved-crackers provided As₂ and Sb

fluxes, while solid-source effusion cells provided Al, Ga, and In fluxes. The growth rates were 0.185 nm s^{-1} for AlSb, 0.185 nm s^{-1} for InAs, and 0.163 nm s^{-1} for GaSb using the following V/III beam equivalent pressure (BEP) ratios: Sb/Al ≈ 20 , As₂/In ≈ 5 , and Sb/Ga ≈ 10 .

Spectroscopic Ellipsometry: Complex reflectance spectra of all samples were measured in air at 45°, 50°, and 55° incidence angles, over a spectral range that included fundamental (1550 nm) and second-harmonic (775 nm) wavelengths, using a spectroscopic ellipsometer (J. A. Woollam Co. model M2000). An iterative nonlinear Levenberg–Marquardt fitting method^[49] yielded optical spectra and layer thicknesses with fitted mean squared errors of ≤ 7 .

Second Harmonic Generation: An Er-doped fiber laser (Calmar Mendocino) with 0.1 ps pulse duration, fundamental wavelength $\lambda = 1.55 \mu\text{m}$, and incident power $\approx 15 \text{ mW}$ was used to excite SHG in the series of structures. The $32 \mu\text{m}$ diameter beam spot was incident on the sample at 40° with variable incoming polarization parallel (p) or normal (s) to the plane of incidence controlled by a zero-order half waveplate following a polarizing beamsplitter cube. The reflected SH beam at $\lambda_{\text{SH}} = 775 \text{ nm}$ was passed through a linear polarizer to isolate individual polarization components p and s before collection at a photomultiplier tube (Hamamatsu, model R10699). A bandpass filter centered at 794 nm and width of 160 nm isolated the final SHG signal.

Supporting Information

Supporting Information is available from the Wiley Online Library or from the author.

Acknowledgements

This work was supported by Robert Welch Foundation grant F-1038. N.D.F. acknowledges additional support from NSF GRFP DGE-1610403, and B.M.S. from CONACyT grant A1-S-9410. A.K.R., J.A.M., and S.R.B. acknowledge support from NSF RAISE-TAQS (Grant Nos. 1838435 and 1839175). The work was partly performed at the Texas Nanofabrication Facility supported by NSF grant NNCI-1542159.

Conflict of Interest

The authors declare no conflict of interest.

Data Availability Statement

The data that support the findings of this study are available from the corresponding author upon reasonable request.

Keywords

digital alloys, ellipsometry, optical second-harmonic generation, quantum wells

Received: December 30, 2021

Revised: March 23, 2022

Published online:

- [1] L. Esaki, R. Tsu, *IBM J. Res. Develop.* **1970**, *14*, 61.
 [2] A. Ramdane, A. Ougazzaden, *Mater. Sci. Eng. B* **2000**, *74*, 66.
 [3] A. Ramdane, F. Devaux, N. El Dahdah, G. Aubin, *Ann. Telecommun.* **2003**, *58*, 1459.

- [4] P. Cristea, Y. Fedoryshyn, J. F. Holzman, F. Robin, H. Jäckel, E. Müller, J. Faist, *J. Appl. Phys.* **2006**, *100*, 116104.
 [5] I. Karabulut, H. Safak, M. Tomak, *J. Appl. Phys.* **2008**, *103*, 103116.
 [6] S. J. Wagner, B. M. Holmes, U. Younis, A. S. Helmy, D. C. Hutchings, J. S. Aitchison, *IEEE Photonics Technol. Lett.* **2009**, *21*, 85.
 [7] L. Alloatti, C. Kieninger, A. Froelich, M. Laueremann, T. Frenzel, K. Köhnle, W. Freude, J. Leuthold, M. Wegener, C. Koos, *Appl. Phys. Lett.* **2015**, *107*, 121903.
 [8] S. J. Maddox, S. D. March, S. R. Bank, *Cryst. Growth Des.* **2016**, *16*, 3582.
 [9] M. Ren, S. Maddox, Y. Chen, M. Woodson, J. C. Campbell, S. Bank, *Appl. Phys. Lett.* **2016**, *108*, 081101.
 [10] E. Delli, P. D. Hodgson, M. Bentley, E. Repiso, A. P. Craig, Q. Lu, R. Beanland, A. R. Marshall, A. Krier, P. J. Carrington, *Appl. Phys. Lett.* **2020**, *117*, 131103.
 [11] L. Persichetti, M. Montanari, C. Ciano, L. D. Gaspare, M. Ortolani, L. Baldassarre, M. Zoellner, S. Mukherjee, O. Moutanabbir, G. Capellini, M. Virgilio, M. D. Seta, *Crystals* **2020**, *10*, 179.
 [12] J. Khurgin, *Phys. Rev. B* **1988**, *38*, 4056.
 [13] P. F. Yuh, K. L. Wang, *J. Appl. Phys.* **1989**, *65*, 4377.
 [14] R. Atanasov, F. Bassani, V. M. Agranovich, *Phys. Rev. B* **1994**, *50*, 7809.
 [15] J. S. Aitchison, M. W. Street, N. D. Whitbread, D. C. Hutchings, J. H. Marsh, G. T. Kennedy, W. Sibbett, *IEEE J. Sel. Top. Quantum Electron.* **1998**, *4*, 695.
 [16] F. Capasso, C. Sirtori, A. Y. Cho, *IEEE J. Quantum Electron.* **1994**, *30*, 1313.
 [17] M. K. Gurnick, T. A. De Temple, *IEEE J. Quantum Electron.* **1983**, *QE-19*, 791.
 [18] A. Fiore, E. Rosencher, V. Berger, J. Nagle, *Appl. Phys. Lett.* **1995**, *67*, 3765.
 [19] S. Houver, A. Lebreton, T. A. Pereira, G. Xu, R. Colombelli, I. Kundu, L. H. Li, E. H. Linfield, A. G. Davies, J. Mangeney, J. Tignon, R. Ferreira, S. S. Dhillon, *Sci. Adv.* **2019**, *5*, eaaw7554.
 [20] I. Saidi, *J. Appl. Phys.* **2019**, *126*, 135704.
 [21] F. De Leonardis, R. A. Soref, *J. Lightwave Technol.* **2022**.
 [22] M. B. Panish, *Science* **1980**, *208*, 916.
 [23] A. N. Semenov, V. A. Solov'ev, B. Y. Meltser, Y. V. Terent'ev, L. G. Prokopova, S. V. Ivanov, *J. Cryst. Growth* **2005**, *278*, 203.
 [24] Y. H. Zhang, *J. Cryst. Growth* **1995**, *150*, 838.
 [25] M. E. Woodson, M. Ren, S. J. Maddox, Y. Chen, S. R. Bank, J. C. Campbell, *Appl. Phys. Lett.* **2016**, *108*, 081102.
 [26] B. C. Juang, B. Liang, D. Ren, D. L. Prout, A. F. Chatziioannou, D. L. Huffaker, *Crystals* **2017**, *7*, 313.
 [27] J. Zheng, Y. Yuan, Y. Tan, Y. Peng, A. K. Rockwell, S. R. Bank, A. W. Ghosh, J. C. Campbell, *J. Lightwave Technol.* **2019**, *36*, 3580.
 [28] G. B. Stringfellow, *J. Appl. Phys.* **1983**, *54*, 404.
 [29] L. G. Vaughn, L. Ralph, H. Xu, Y. Jiang, L. F. Lester, *MRS Online Proc. Libr.* **2002**, *744*, M7.2.
 [30] Y. G. Hong, A. Y. Egorov, C. W. Tu, *J. Vac. Sci. Technol. B: Microelectron. Nanometer Struct.* **2002**, *20*, 1163.
 [31] R. Kaspi, G. P. Donati, *J. Cryst. Growth* **2003**, *251*, 515.
 [32] Y. Lyu, X. Han, Y. Sun, Z. Jiang, C. Guo, W. Xiang, Y. Dong, J. Cui, Y. Yao, D. Jiang, G. Wang, Y. Xu, Z. Niu, *J. Cryst. Growth* **2018**, *482*, 70.
 [33] A. K. Rockwell, M. Ren, M. Woodson, A. H. Jones, S. D. March, Y. Tan, Y. Yuan, Y. Sun, R. Hool, S. J. Maddox, M. L. Lee, A. W. Ghosh, J. C. Campbell, S. R. Bank, *Appl. Phys. Lett.* **2018**, *113*, 102106.
 [34] X. Yi, S. Xie, B. Liang, L. W. Lim, J. S. Cheong, M. C. Debnath, D. L. Huffaker, C. H. Tan, J. P. David, *Nat. Photonics* **2019**, *13*, 683.
 [35] R. L. Restrepo, J. P. González-Pereira, E. Kasapoglu, A. L. Morales, C. A. Duque, *Opt. Mater.* **2018**, *86*, 590.
 [36] S. Yadav, A. B. Bhattacharjee, *Phys. Scr.* **2022**, *97*, 015102.
 [37] D. S. Bethune, *J. Opt. Soc. Am. B* **1989**, *6*, 910.

- [38] G. Berkovic, G. Marowsky, R. Steinhoff, Y. R. Shen, *J. Opt. Soc. Am. B* **1989**, 6, 205.
- [39] R. Stolle, G. Marowsky, E. Schwarzberg, G. Berkovic, *Appl. Phys. B: Lasers Opt.* **1996**, 63, 491.
- [40] R. W. Boyd, *Nonlinear Optics*, 2nd edition, Elsevier, Burlington **2003**.
- [41] H. Hardhienata, A. Alejo-Molina, C. Reitböck, A. Prylepa, D. Stifter, K. Hingerl, *J. Opt. Soc. Am. B* **2016**, 33, 195.
- [42] R. W. Hollering, *Opt. Commun.* **1992**, 90, 147.
- [43] D. Teshima, R. Fujimura, K. Kajikawa, *Jpn. J. Appl. Phys.* **2014**, 53, 032202.
- [44] A. Aktsipetrov, I. Baranova, A. Il'inskii, *J. Exp. Theor. Phys.* **1986**, 91, 287.
- [45] S. Adachi, *J. Appl. Phys.* **1989**, 66, 6030.
- [46] M.-Z. Huang, W. Ching, *Phys. Rev. B* **1993**, 47, 9464.
- [47] C. Nguyen, B. Brar, H. Kroemer, *J. Vac. Sci. Technol. B: Microelectron. Nanometer Struct.* **1993**, 11, 1706.
- [48] G. Lüpke, *Surf. Sci. Rep.* **1999**, 35, 75.
- [49] W. H. Press, B. P. Flannery, S. A. Teukolsky, W. T. Vetterling, *Numerical Recipes: The Art of Scientific Computing*, Cambridge University Press, Cambridge, MA **1988**.